



**HAL**  
open science

# Towards the Improvement of the Short-Loop Recycling of Dy-Rich Nd-Fe-B Permanent Magnets: Experimental and Numerical Approaches

Gatien Bacchetta, Sorana Luca, Cyril Rado, Frederico Orlandini Keller,  
Jean-Paul Garandet

## ► To cite this version:

Gatien Bacchetta, Sorana Luca, Cyril Rado, Frederico Orlandini Keller, Jean-Paul Garandet. Towards the Improvement of the Short-Loop Recycling of Dy-Rich Nd-Fe-B Permanent Magnets: Experimental and Numerical Approaches. *Advanced Engineering Materials*, 2024, 26 (9), pp.2400234. 10.1002/adem.202400234 . cea-04850130

**HAL Id: cea-04850130**

**<https://cea.hal.science/cea-04850130v1>**

Submitted on 31 Dec 2024

**HAL** is a multi-disciplinary open access archive for the deposit and dissemination of scientific research documents, whether they are published or not. The documents may come from teaching and research institutions in France or abroad, or from public or private research centers.

L'archive ouverte pluridisciplinaire **HAL**, est destinée au dépôt et à la diffusion de documents scientifiques de niveau recherche, publiés ou non, émanant des établissements d'enseignement et de recherche français ou étrangers, des laboratoires publics ou privés.



Distributed under a Creative Commons Attribution - NonCommercial - NoDerivatives 4.0 International License

# Toward the Improvement of the Short-Loop Recycling of Dy-Rich Nd–Fe–B Permanent Magnets: Experimental and Numerical Approaches

Gatien Bacchetta,\* Sorana Luca, Cyril Rado, Frederico Orlandini-Keller, and Jean-Paul Garandet

The method of short-loop recycling of Nd–Fe–B magnets is implemented, with end-of-life (EoL) magnets used as a source of heavy rare earth (HRE). Partially recycled magnets are fabricated by co-sintering HRE-free powders obtained from strip casted alloys, blended with HRE-rich powders obtained from EoL magnets. The impact of several process parameters (blending ratio, sintering cycle, and HRE-rich recycled particle sizes) on the microstructure and magnetic properties is discussed. A coercivity gain up to  $160 \text{ kA m}^{-1} \text{ wt}\%^{-1}$  of Dy with respect to the HRE-free magnets is reported, even though impurities are incorporated. Microstructural characterizations show a heterogeneous Dy localization in core-shell/anticore-shell structures, and thus a nonoptimal use of HRE. The experimental results are compared with finite element simulations of the Dy diffusion transport performed using existing data of bulk Dy diffusion coefficients. The simulation model consists of a network of square grains separated by a liquid phase, whose fraction is based on the ternary Nd–Fe–B phase diagram. Results show similarities with the observed microstructures, and point to the interest of reducing the Dy-rich particle size with respect to the main powder. This study provides new insights into the Dy transport mechanisms at stake in an efficient short-loop recycling of HRE.

## 1. Introduction

Since their discovery in 1984,<sup>[1,2]</sup> anisotropic Nd–Fe–B sintered permanent magnets hold the record for the highest maximum energy product  $(BH)_{\text{max}}$ .<sup>[3]</sup> They find applications in many industrial fields such as traction motors of electric vehicles (EVs) and hybrid electric vehicles (HEVs), or wind turbines. The forecasted


growth of the use of these technologies<sup>[4]</sup> points to an increase of the economic importance of Nd–Fe–B sintered magnets. However, a potential obstacle to their development is that they contain typically 30–32 wt% of rare earths (RE), considered as critical or very critical, respectively, for light rare earths (LRE) and heavy rare earths (HRE).<sup>[5]</sup>

The RE crisis in 2011 led many research groups to develop recycling methods for these materials. Among them, the so-called magnet to powder<sup>[6]</sup> short-loop recycling methods have been proposed by Rivoirard et al.<sup>[7]</sup> and Zakotnik et al.<sup>[8]</sup> From end-of-life (EoL) magnets, hydrogen decrepitation (HD) followed or not by hydrogenation disproportionation desorption recombination processes results in an anisotropic magnetic powder which can be used for the fabrication of bonded magnets.<sup>[9–18]</sup> After HD, it is furthermore possible to produce anisotropic sintered magnets by tuning the standard powder metallurgy route.<sup>[8,19–29]</sup> Short-loop recycled

materials contain impurities, such as C, O, or N, originating from the scrap magnet and hard to remove from the material.<sup>[21]</sup> To prevent a loss of magnetic properties due to the formation of undesired phases (RE oxides, carbides) and closed porosities after the recycling process, additional elements such as RE hydrides<sup>[21,28]</sup> or intermetallics<sup>[23,25,27]</sup> can be mixed with the recycled powder before sintering. These methods showed promising results even at the industrial scale<sup>[25,30]</sup> while being as well very energy efficient compared to the elemental recovering of RE.<sup>[6]</sup>

Another context element is that HEVs, EVs, and wind turbines applications require magnets with high coercivity at room temperature ( $H_c$ ) so that they can withstand the application conditions without a permanent flux loss.<sup>[3]</sup> The addition of HRE, such as Dy or Tb, to the magnet alloy is a well-known approach to enhance the coercivity of Nd–Fe–B magnets at room temperature. The main reason is that the magnetocrystalline anisotropy of the  $\text{Nd}_2\text{Fe}_{14}\text{B}$  phase ( $\varphi$  phase) is enhanced if Nd is partially substituted by a HRE.<sup>[31]</sup> But this substitution decreases the saturation magnetization due to antiferromagnetic coupling between Fe and HRE atoms,<sup>[31]</sup> hence decreasing the remanence ( $B_r$ ) and the maximum energy product  $(BH)_{\text{max}}$ .<sup>[32]</sup> Besides, HRE

G. Bacchetta, S. Luca, C. Rado, F. Orlandini-Keller, J.-P. Garandet  
Univ. Grenoble Alpes, CEA, LITEN, DTNM  
38000 Grenoble, France  
E-mail: gatién.bacchetta@cea.fr

 The ORCID identification number(s) for the author(s) of this article can be found under <https://doi.org/10.1002/adem.202400234>.

© 2024 The Authors. Advanced Engineering Materials published by Wiley-VCH GmbH. This is an open access article under the terms of the Creative Commons Attribution-NonCommercial-NoDerivs License, which permits use and distribution in any medium, provided the original work is properly cited, the use is non-commercial and no modifications or adaptations are made.

DOI: 10.1002/adem.202400234

are even less abundant and more expensive than LRE explaining why many studies have been carried out on the overall reduction of their amount by the optimal utilization of the resource. One method is the grain boundary diffusion process (GBDP) which consists of a postsintering diffusion treatment of HRE from the surface of a magnet using a HRE-based compound.<sup>[33]</sup> This allows to form a so-called core-shell structure, with grains of the  $\phi$  phase having a partially substituted HRE-rich shell surrounding a HRE-free core. As opposed to processes leading to an homogeneous distribution of HRE in the  $\phi$  phase, a high magnetocrystalline anisotropy is thus induced only in the vicinity of grain boundaries, reinforcing the region where the  $\phi$  phase crystals are more likely to present defects and to nucleate and propagate reverse domains under a reverse applied field.<sup>[34]</sup> This method allows an impressive coercivity enhancement with a very small decrease in remanence because of a minimal use of HRE.<sup>[35–41]</sup> However, this GBDP technique results in a heterogeneous microstructure at magnet scale, with a surface richer in HRE than the center of the magnet.<sup>[33]</sup> Even though recent studies showed that a separate diffusion treatment could reduce these magnet-scale heterogeneities,<sup>[36,42]</sup> the GBDP technique is limited to the production of magnets with thicknesses below 1 cm.

Another fabrication method is to use powder-blend or dual alloy techniques, which involve typically a HRE-free Nd-Fe-B alloy mixed with HRE-rich powders (HRE hydrides, oxides, sulfide, and fluorides,<sup>[43–48]</sup> or intermetallics<sup>[23,49,50]</sup>). Contrary to GBDP, the core-shell microstructure formed during sintering is homogeneously distributed at the magnet scale. As a result, coercivity is enhanced while maintaining a high remanence and magnet size is not limited by the diffusion length of Dy along grain boundaries. To avoid microstructural and compositional heterogeneities at a few grains scale, it is more convenient to use HRE-rich alloys having a composition close to a Nd-Fe-B magnet, also called Multi Main Phase (MMP) methods.<sup>[34,51–59]</sup> Several authors report on the implementation of this process using recycled material as a source of HRE,<sup>[22,29,60]</sup> as well as the formation of core-shell-type structures.<sup>[22]</sup>

The formation mechanism of Dy shells during GBDP or MMP is still a subject of scientific controversy and at least three different mechanisms have been proposed so far. A common feature of these methods is that the processes take place at temperatures above the first eutectic  $L \leftrightarrow \text{Nd} + \text{Nd}_2\text{Fe}_{14}\text{B} + \text{Nd}_{1.1}\text{Fe}_4\text{B}_4$  which is typically ranging between 650 and 750 °C depending on the additive elements used.<sup>[37]</sup> This leads to the formation of a liquid phase partially wetting solid grains<sup>[61]</sup> allowing a long-range transport of Dy along the grains. Nakamura et al.<sup>[62]</sup> proposed a dual liquid and solid-state diffusion mechanism to explain the formation of core-shell microstructures which is still used in recent works.<sup>[38,40,63–67]</sup> However, sharp and faceted interfaces are commonly observed between the core and the shell,<sup>[58,68–70]</sup> which is not consistent with a diffusion-like process. To account for such an observation, Oono et al.<sup>[70]</sup> proposed a mechanism suggesting that Dy shells were formed after solidification of partially melted grains. It has also been tried to correlate the liquid phase fraction calculated with thermodynamic data with the actual volume fraction of the shells.<sup>[68]</sup> But the liquid phase fractions are too low to totally account for the thickness of the shells formed for a standard surface diffusion treatment. A new mechanism of chemically induced

liquid film migration (CILFM) was proposed by Kim et al.<sup>[69]</sup> consisting in grain boundary migration followed by a faceted solidification of shells and coarsening of grains. This mechanism allowed an adequate interpretation of some of the concentrations profiles in a recent study of Wang et al.<sup>[35]</sup> But to the best of our knowledge, no fully clear picture emerges from the literature, and it can be thought that all these mechanisms coexist or act in sequence depending on the local thermodynamic and process environment.

Judging from the growing interest for the use of recycled materials and for the reduction of the HRE content, our objective in the present work is to use recycled magnets as the only source for HRE for the fabrication of high-performance NdFeB magnets. More precisely, a powder-blend method is implemented with HRE-rich EoL magnets and a specially designed HRE-free strip casted alloy with the aim to produce a homogeneous repartition of core-shell-type grains in the microstructure at magnet scale. To do so, the influence of the mixing ratios, sintering cycles, and the use of two different mean particle sizes for recycled material are evaluated. Then, microstructural analysis will allow a better understanding of the magnetic properties, as well as the Dy transport mechanisms at stake. To gain further insights on these transport issues and allow a discussion of the experimental observations, we also perform finite element diffusion simulations that takes into account existing data for the diffusion coefficients of Dy and thermodynamic data for the Nd-Fe-B ternary system.

## 2. Results

### 2.1. Magnetic Properties and Impurities

This section covers the influence of several process parameters on the magnetic properties of the fabricated magnets, with SC-M1 and SC-M2 blends. The M1 batch has a mean particle size similar to the grain size of the initial EoL magnet. In order to decrease the Dy diffusion lengths from the recycled powder to the HRE-free grains, we reduced the mean particle size distribution of the M2 HRE-rich recycled powder, as done previously in a recent work by Opelt et al.<sup>[54]</sup> In a first series of experiments, the compacts produced with recycled powder ratios ranging from 0 to 50 wt% were sintered at 1000 °C–4 h and annealed according to the procedure described in Section 5. The corresponding weight percentages of Dy are listed in **Table 1**, together with the measured remanence, coercivity, and apparent densities. Theoretical density is considered to be  $7.5 \text{ g cm}^{-3}$ <sup>[31]</sup> so full densification can be considered to be achieved in all cases, given the  $\pm 0.06 \text{ g cm}^{-3}$  uncertainty. **Figure 1a,b** shows the demagnetization curves of several partly recycled magnets for the SC-M1 (a) and SC-M2 (b) batches, which all feature significant improvements with respect to HRE-free SC materials.

In a second series of experiments, we varied the sintering temperature and adjusted the sintering dwell duration to limit Dy diffusion kinetics. A first result to be mentioned is that these modified conditions did not affect the density of the sintered magnets, which remained at  $7.5 \text{ g cm}^{-3}$  within the experimental uncertainty. **Figure 1c,d** shows remanence, room temperature coercivity, and squareness (SQ) factor as a function of the

**Table 1.** Magnetic properties and apparent densities depending on the recycled powder fraction with their corresponding Dy fraction. Sintering was performed at 1000 °C–4 h and annealing at 800–520 °C.

	Recycled powder [wt%]	Dy [wt%]	$B_r$ [ $\pm 0.04$ T]	$H_{cJ}$ [ $\pm 30$ kA m $^{-1}$ ]	Density [ $\pm 0.06$ g cm $^{-3}$ ]
SC-M1	0	0	1.28	1360	7.54
	10	0.4	1.30	1440	7.53
	25	1.1	1.28	1530	7.52
	30	1.4	1.28	1550	7.52
	50	2.3	1.25	1640	7.54
SC-M2	0	0	1.28	1360	7.54
	10	0.4	1.30	1420	7.54
	25	1.1	1.29	1500	7.54
	30	1.4	1.28	1540	7.54
	50	2.3	1.25	1630	7.50

**Table 2.** Coercivity gain per Dy unit mass, obtained by linear regression, after annealing depending on the sintering cycle and the particle size distribution of the jet milled EoL magnet.

Sintering conditions	$\Delta H_{cJ}/Dy$ [kA m $^{-1}$ wt% $^{-1}$ ]	
	SC-M1	SC-M2
975 °C–6 h	112 $\pm$ 17	104 $\pm$ 20
1000 °C–4 h	110 $\pm$ 15	121 $\pm$ 10
1050 °C–4 h	160 $\pm$ 30	–

recycled powder fraction in the annealed partly recycled magnet for several sintering conditions (975 °C–6 h, 1000 °C–4 h, 1050 °C–4 h) for SC-M1 batch (c) and SC-M2 batch (d). Coercivity gains per weight fraction of Dy are listed for each

condition in Table 2. The coercivity enhancement per wt% of Dy is surprisingly similar for each condition, except for a sintering at 1050 °C–4 h, which exhibits a slightly better coercivity gain. The SQ factor is quite stable with the recycled powder fraction; however, it clearly decreases with the decrease of the sintering temperature. We can also observe that magnets fabricated with SC-M2 batch exhibit a slightly lower SQ factor compared to SC-M1 batch, especially at high mixing ratio. The remanence is slightly decreased with the mixing ratio due *inter alia* to the enhancement of the Dy content which decreases the saturation magnetization of the  $\phi$ -phase.<sup>[31]</sup>

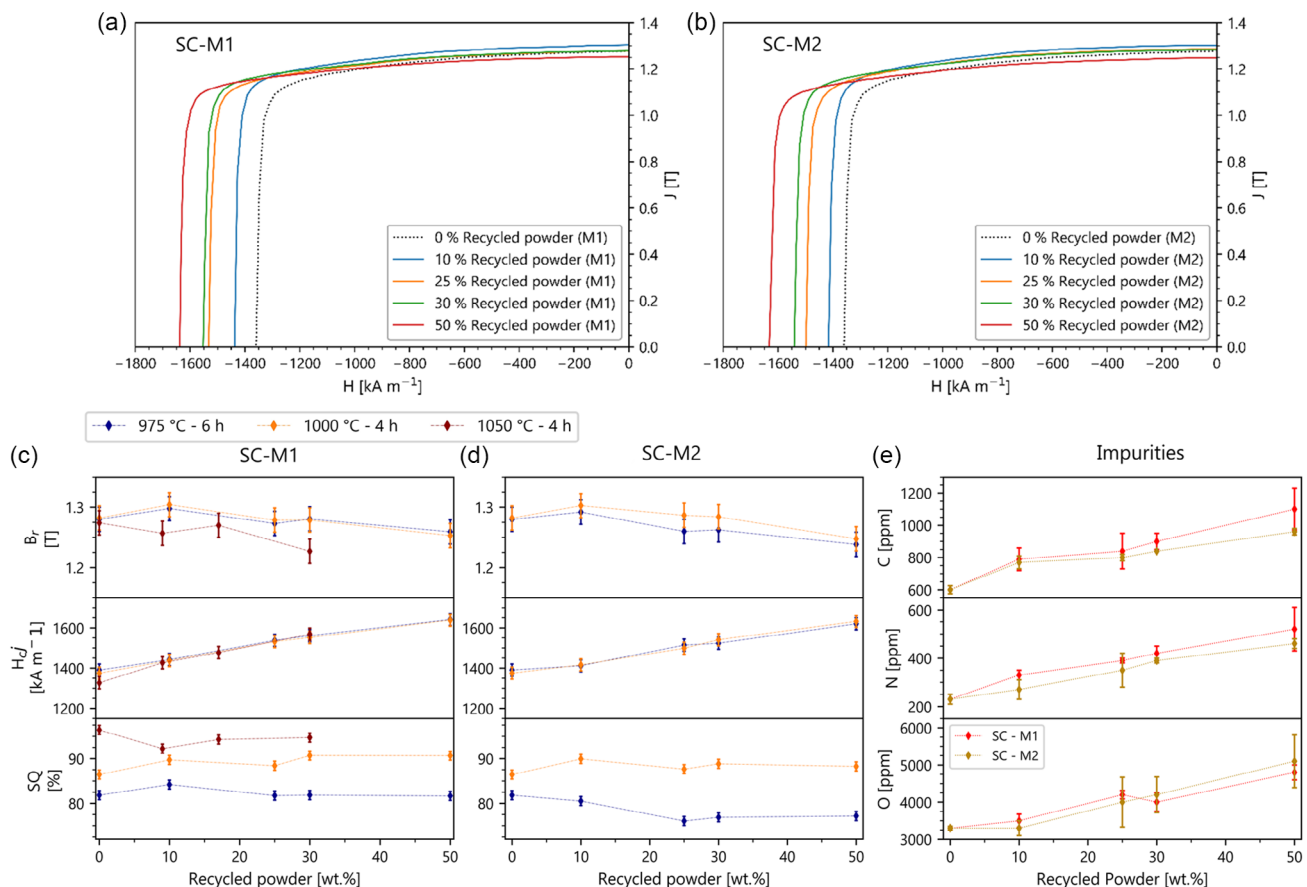


**Figure 1.** Demagnetization curves of partly recycled anisotropic sintered magnets of a) SC-M1 and b) SC-M2 batches, sintering at 1000 °C–4 h and annealing at 800–520 °C. Remanence, room temperature coercivity, and SQ factor, as a function of the recycled powder fraction in the annealed partly recycled magnet for several sintering conditions (975 °C–6 h, 1000 °C–4 h, 1050 °C–4 h) for c) SC-M1 and d) SC-M2 batches. e) O, N, and C contents in the partly recycled magnets of SC-M1 and SC-M2 batches.



Using recycled materials as a source of Dy induces an increase of the impurity levels in the final magnets. Figure 1e depicts the O, N, and C levels in the partly recycled magnets. The level of all three impurities increases monotonically with the recycled powder fraction regardless of powder particle size. EoL magnets contain 3 times more carbon and 20 times more nitrogen and oxygen than the Dy-free alloy obtained by strip casting. In addition, the use of a lubricant for the jet milling and orientation stages increases the C and O content. The N-level increase is associated with its incorporation during jet milling. No clear difference on the contamination levels was evidenced between the 5 and 3.5  $\mu\text{m}$  batches.

## 2.2. Microstructural Analysis: Homogeneity, Grain Sizes, and Dy Repartition in the Matrix

Figure 2 shows the microstructure of the magnets fabricated with 70 wt% SC–30 wt% M1 (Figure 2a,b) and 70 wt% SC–30 wt% M2 (Figure 2c,d). In both cases, the investigated area covers circa 400 grains. Dark contrast represents the  $(\text{Nd-Pr-Dy})_2\text{Fe}_{14}\text{B}$  phase (or  $\phi$  phase), white contrast are RE-rich phases, and gray contrast are RE oxides. The Dy elemental maps allow us to identify recycled grains (marked with yellow circles) surrounded by SC powder grains (marked with yellow triangle). Recycled grains are quite homogeneously distributed in the matrix even though some of the Dy-rich grains are locally agglomerated.

The effect of the mean recycled powder size addition on magnet grain size was estimated with surface analysis of polished cross sections of 70 wt% SC–30 wt% M1 and 70 wt% SC–30 wt% M2 magnets sintered at 1000  $^\circ\text{C}$ –4 h and compared to SC reference magnet (Figure 2e). The grain sizes appear similar than particle sizes after jet milling (Figure 7b), however they cannot directly be compared due to the differences between

the measurement techniques. Grain sizes are derived on microstructural images from the diameters of the disks within the measured section, and mathematically corrected to match with the spatial diameter of the corresponding tetradecahedron (see the characterization procedure in Section 5). The data are quite scattered, but the main conclusion is that the grain distribution is similar in all cases, even though the slightly smaller mean for the SC-M2 magnet could tentatively be seen as the trace of the smaller grain size after jet milling in that batch.

The Dy elemental maps and concentration profiles at the scale of several grains are shown in Figure 3a–e for 30% recycled powder magnets sintered at 975  $^\circ\text{C}$ –6 h and annealed with the SC-M1 batch (a,c) and SC-M2 batch (b,d). Dark contrasts are  $\phi$  phases and bright contrasts are Nd-rich phases (including oxides). Data from Dy-rich grains, which belong to the initial recycled powder grains, clearly show a faceted anticore–shell structure, with a Dy-poor shell surrounding a Dy-rich core. The SC powder grains exhibit a thin Dy-rich shell, and it is more noticeable for the magnet fabricated with the SC-M2 batch compared to the SC-M1 batch. However, the concentration profiles shown in Figure 3e do not show a sharp Dy enrichment in the vicinity of the main powder grains due mainly to poor signal-to-noise ratio. The sharp interfaces visible on the backscattered electron (BSE) images seem to diminish on the Dy concentration profile mainly because of the electron–matter interaction volume at 10 kV, estimated to be around 0.4  $\mu\text{m}$ , which is of the same order of magnitude as the Dy rich-shell.

SC-M1 magnets sintered at 1050  $^\circ\text{C}$ –4 h exhibit a slightly higher gain in coercivity per wt% of Dy (see Table 2). A series of energy-dispersive X-ray spectroscopy (EDS) point analysis in the core of  $\text{Nd}_2\text{Fe}_{14}\text{B}$  grains of the EoL magnet M and magnets sintered at 1050  $^\circ\text{C}$ –4 h with SC batch and SC-M1 batch allowed

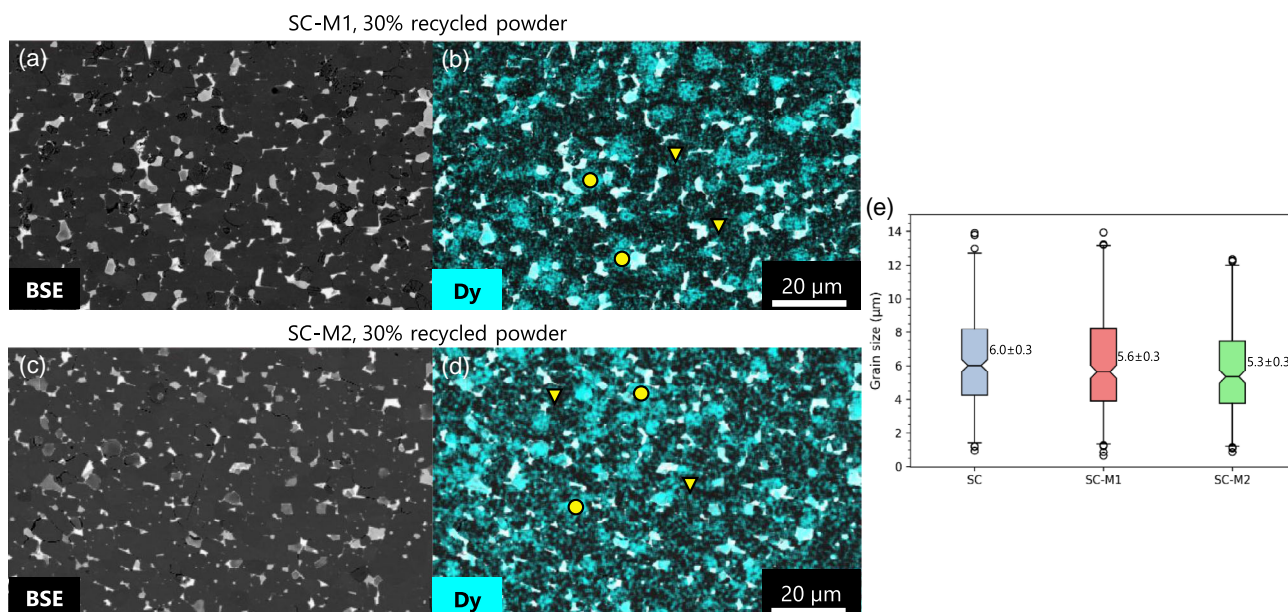


**Figure 2.** Microstructure of a 30% recycled powder magnets fabricated with a,b) SC-M1 and c,d) SC-M2 blends, sintered at, respectively, 975  $^\circ\text{C}$ –6 h and 1000  $^\circ\text{C}$ –4 h, annealed at 800–520  $^\circ\text{C}$ . (a,c) BSE images. (b,d) BSE images superimposed with Dy elemental map. e) Grain size evolution for reference magnet SC and 30% recycled SC-M1 and SC-M2 magnets sintered at 1000  $^\circ\text{C}$ –4 h. Medians are marked for each set of measurement, notches represent the 95% confidence interval around the median, lower whisker is 1%, and upper whisker is 99%. Black circles are extreme data points.

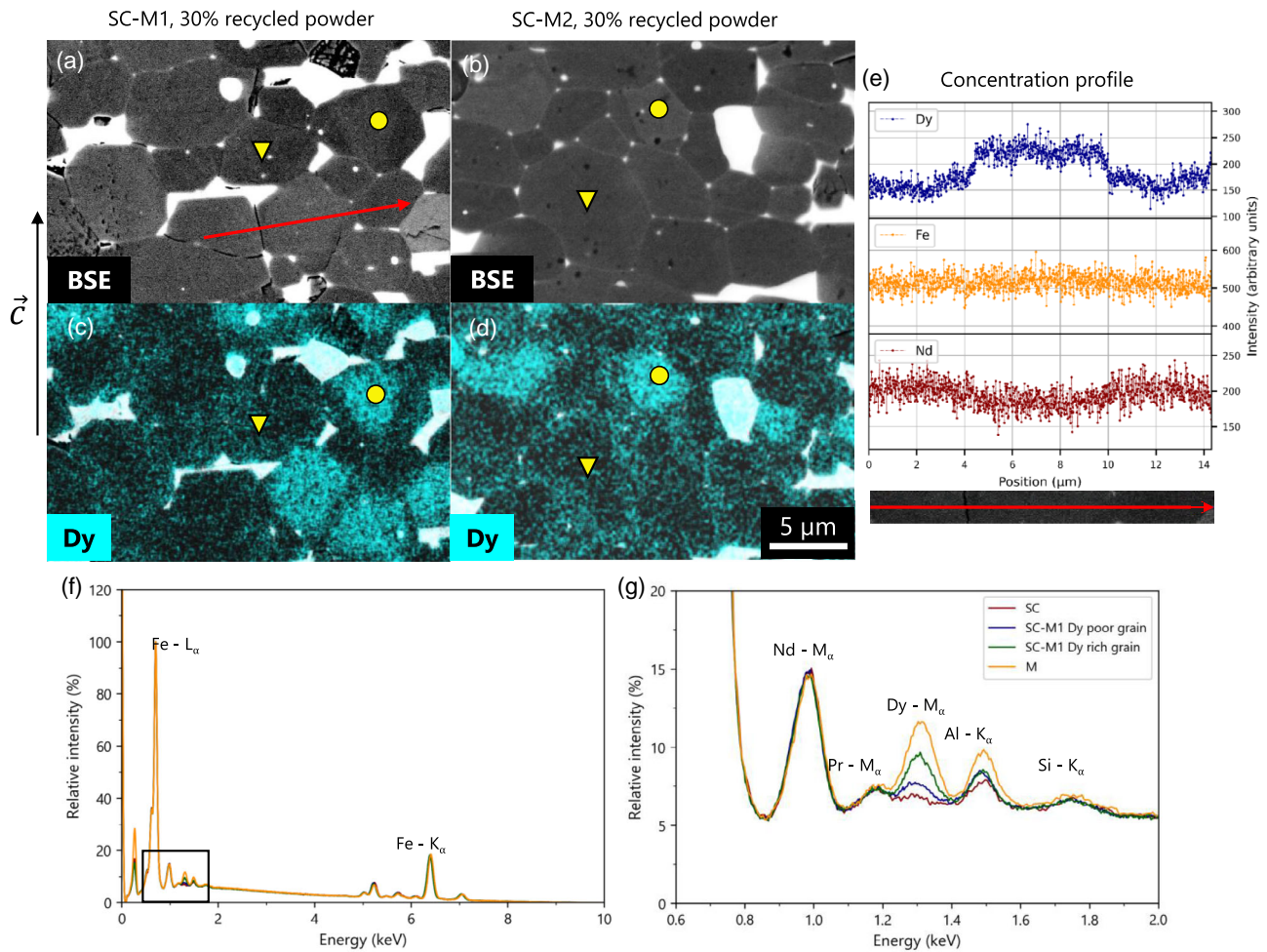


**Figure 3.** Microstructure of a 30% recycled powder magnet sintered at 975 °C–6 h and annealed at 800–520 °C with the a,c) SC-M1 batch and b,d) SC-M2 batch. (a,b) BSE images (dark contrasts : Nd<sub>2</sub>Fe<sub>14</sub>B phase, white contrast : Nd-rich phases. (c,d) BSE images superimposed with Dy elemental map. e) Concentration profiles of Dy, Fe, Nd across a Dy-enriched grain. Each picture is given with a vertical easy magnetization *c*-axis. f) EDS spectra of Nd<sub>2</sub>Fe<sub>14</sub>B phase in a SC reference magnet (0% recycled), a Dy-poor grain and, a Dy-rich grain in a 30% recycled magnet SC-M1 and in the initial magnet M. Magnets were sintered at 1050 °C–4 h and annealed at 850–520 °C except for the initial magnet M which was taken as it was. Si signal is a polishing artefact. g) Magnification of the inset in (f).

us to gain some insights on the amount of Dy that has been transported from the grains issued from recycled powder to the SC powder grains. For this analysis, a set of 5–7 grains of the  $\phi$  phase were analyzed. The corresponding average EDS spectra for these samples are plotted in Figure 3f,g for Dy-rich and Dy-poor grains which were recorded separately. A quantitative composition analysis with a reference sample was not performed on these experiments, but we can still conclude that the Dy concentration has started to homogenize during sintering because Dy peaks of SC-M1 grains are between the M and SC peaks. However, the total homogenization of the concentration is not reached because it is still possible to discriminate Dy-poor and Dy-rich grains. As for Al, its peaks from the SC-M1 grains are also between the M and SC peaks, but no significant difference is observed between Dy-rich and Dy-poor grains. This points to a complete homogenization, which can tentatively be ascribed to a faster diffusivity for Al with respect to Dy.

### 2.3. Diffusion Simulations

Diffusion simulations were performed for several sintering temperatures (between 900 °C and 1100 °C) and durations (from 0 to 12 h) to bring new insights on the observed microstructural features. **Figure 4** shows the Dy concentration evolution at similar time locations on four square grains at  $t=0$  (a),  $t=1$  h (b),  $t=4$  h (c), and  $t=12$  h (d) for an equivalent temperature of 1000 °C using the 5  $\mu\text{m}$  geometry and the 2.5  $\mu\text{m}$  geometry (respectively Figure 4e–h). For each case, the Dy in the initial Dy-rich grain diffuses from its periphery into the liquid phase, where Dy concentration is spatially homogeneous. Concerning the 5  $\mu\text{m}$  geometry at  $t=1$  h (Figure 4b), an anticore–shell type structure is visible and correlated to a core–shell microstructure in initially Dy-free grains. The same trend is observed in the 2.5  $\mu\text{m}$  geometry (Figure 4e–h), but the concentration at the core of initially Dy-rich grains is lower than the one in the 5  $\mu\text{m}$

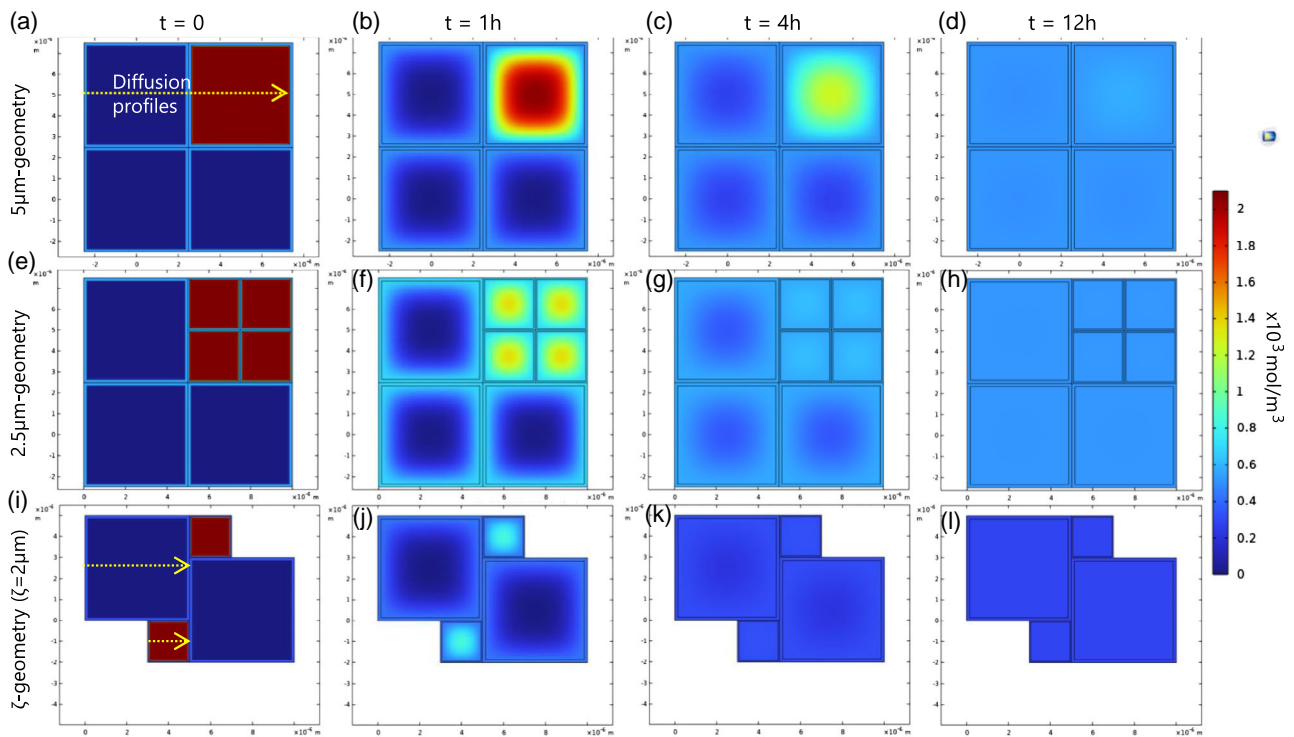


**Figure 4.** Dy concentration evolution at 1000 °C for a,e)  $t = 0$ , b,f)  $t = 1$  h, c,g)  $t = 4$  h, and d,h)  $t = 12$  h with the (a–d) 5  $\mu\text{m}$  geometry, the (e–h) 2.5  $\mu\text{m}$  geometry, and the i–l)  $\zeta$  geometry with  $\zeta = 2$   $\mu\text{m}$ . Yellow arrows show the position of the diffusion profiles. For animated views of this figure, the reader is referred to the supporting information given with this article (Figure S1–S6, Supporting Information).

geometry, indicating a much faster Dy transport. When the thermal treatment duration is increased, Dy concentration tends to homogenize to reach a uniform distribution, as shown in Figure 4d,h, for 12 h of dwell time.

From the point of view of an efficient use of Dy from EoL magnets, the appearance of anticore–shells structures is problematic for industrial applications because anticore–shell structures are known to be preferential sites for reverse stray fields which has a deleterious impact on coercivity.<sup>[71]</sup> Besides, the existence of anticore–shell structures implies that a significant quantity of critical HRE remains stuck in the initial Dy-rich grains, pointing to a non-optimal use of the resource. On a more positive line, the numerical results hint that finer Dy rich particles could potentially solve this problem. Thus, we performed additional simulations to calculate the maximum required particle size to obtain the core–shell desired microstructures without the appearance of the anticore–shell structures. More precisely, the  $\zeta$  geometry allows a variation of the Dy-rich particle size  $\zeta$ . The results for an equivalent sintering temperature of 1000 °C are shown in Figure 4 for  $\zeta = 2$   $\mu\text{m}$  with durations of  $t = 0$  (i),  $t = 1$  h (j),  $t = 4$  h (k), and  $t = 12$  h (l). Contrary to the previous geometries, the total amount of Dy diffusing depends on  $\zeta$  which is why the equilibrium concentration at the end of the thermal treatment is lower for  $\zeta = 2$   $\mu\text{m}$  than for the previous geometries. We see that for  $\zeta = 2$   $\mu\text{m}$ , at  $t = 1$  h, the concentration in the small grains is more homogeneous whereas the large grains have a clear core–shell effect.

Diffusion profiles were extracted on the lines showed in yellow in Figure 4a (5  $\mu\text{m}$  geometry) and Figure 4i ( $\zeta = 2$   $\mu\text{m}$ ). They are

plotted for an equivalent temperature of 950 °C (a,b) and 1050 °C (c,d) in Figure 5. Note here that the profiles based on  $\zeta$  geometry are the result of the concatenation of Dy-rich and Dy-poor profiles. Higher temperature increases the diffusion kinetics and thus induces a faster penetration of Dy in initially Dy-poor grains. As the 5  $\mu\text{m}$  geometry is highly symmetrical (same grain sizes), we notice a quite symmetric behavior between the Dy-rich and Dy-poor grain. Between the two grains, the concentration in the liquid is constant all along the heat treatment and equal to the fourth of the initial concentration in the Dy-rich grain for the 5  $\mu\text{m}$  geometry. On the other hand, Dy concentration in the liquid in the  $\zeta = 2$   $\mu\text{m}$  is decreasing with the increasing diffusion time. A higher temperature also increases the liquid phase fraction, but in the tested ranges (13–19% of liquid phase) it has no clear influence on the diffusion kinetics.

To analyze the link between a given concentration map and the diffusion time/temperature couples, we analyzed the diffusion profiles firstly on the 5  $\mu\text{m}$  geometry in the Dy-poor grains, keeping in mind that in such a geometry a favorable core–shell structure in Dy-poor grains is necessarily correlated with an unfavorable anticore–shell structure in Dy-rich grains. The characteristic penetration distance  $d$  is defined from the intersection of the tangent of the concentration profile at the solid/liquid interface with the  $x$ -axis (Figure 6a,b), and can be compared to  $d_{\text{middle}}$ , the distance between the liquid/solid interface and the center of the grain. Considering that  $d < d_{\text{middle}}$  corresponds to a core–shell (Figure 6a) microstructure and  $d > d_{\text{middle}}$  corresponds to a homogeneous distribution (Figure 6b), a master curve  $d = d_{\text{middle}}$



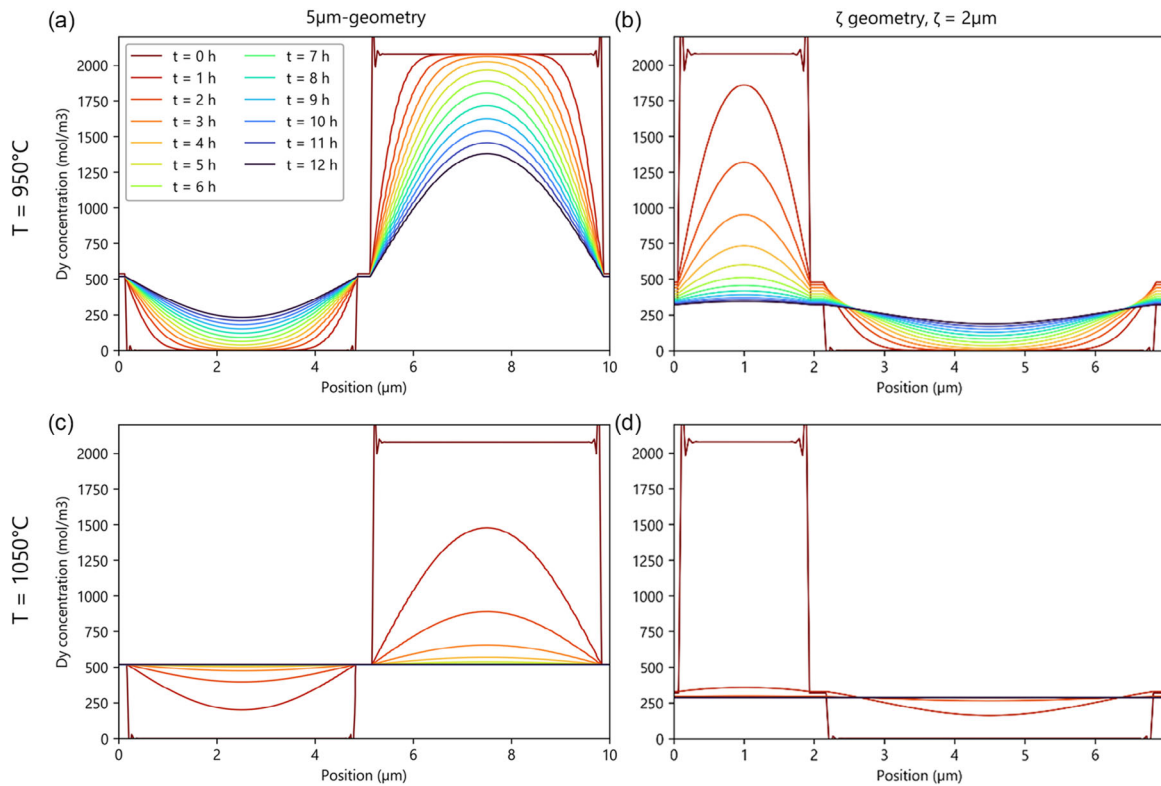


**Figure 5.** Dy concentration profiles on a, c) 5 μm geometry, ζ geometry with b, d) ζ = 2 μm at 950 °C (a, b) and 1050 °C (c, d) for t ranging from 0 to 12 h.

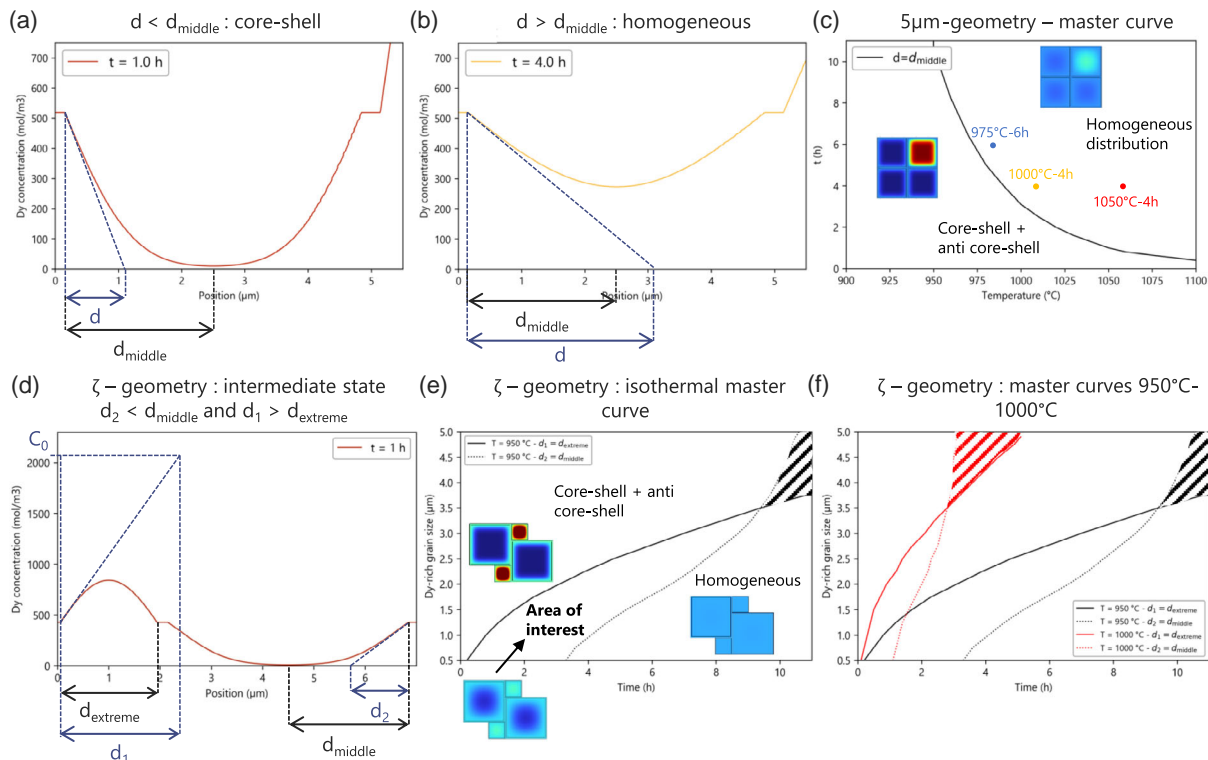


**Figure 6.** Dy concentration at 1000 °C for a) t = 1 h and b) t = 4 h with diffusion lengths  $d$  and  $d_{middle}$  displayed. c) Borders between the homogeneous and the core-shell + anticore-shell domains for the 5 μm geometries. d) Criterion used for the area of interest of the ζ geometry (ζ = 2 μm, T = 1000 °C). e) Isothermal master curves of the ζ geometries for a temperature of 950 °C. f) Effect of temperature (950 and 1000 °C) on master curves.



can be plotted to separate the time/temperature combination microstructural between these two regimes (Figure 6c). The experimental points shown previously are also reported on this curve. Note here that the separation between the domains is based only on the previous criterion. An important feature of this figure is that the experimental points 975 °C–6 h and 1000 °C–4 h are closer from the master curve than the 1050 °C–4 h point. It means that the concentration gaps are sharper for these two configurations.

For application purposes, a configuration allowing to diffuse the majority of the Dy initially present in Dy-rich particles while keeping only a core–shell on the initially Dy-free grain could be considered as ideal. While this is obviously not possible in symmetrical geometries (see, e.g., the 5 μm case in Figure 4a–d), it is a priori interesting to test whether ζ geometries allow to approach this ideal configuration. To do so, we can use again the same comparison criterion for the Dy-poor grains, with the distance  $d_2$  compared to  $d_{\text{middle}}$  in the same way that for the 5 μm geometry (Figure 6d). On the other hand, in the Dy-rich grains, the characteristic distance  $d_1$  taken from the intersection of the concentration profile tangent at the solid/liquid interface with its initial concentration  $C_0$  is compared to  $d_{\text{extreme}}$  which is the distance between the two solid/liquid interfaces. The set of ζ geometry/time/temperature parameters, which satisfy the above defined ideal configuration criterion, are considered to be the area of interest. The corresponding isothermal master curves of the ζ geometries are shown in Figure 6e for a fixed temperature of 950 °C. At a given temperature, the border between the area of interest and the core–shell + anticore–shell domains is represented by the time for which  $d_1 = d_{\text{extreme}}$ , whereas the border between the area of interest and homogeneous domains is represented by the time for which  $d_2 = d_{\text{middle}}$ . For a Dy-free powder grain size of 5 μm, calculations show that the existence of an area of interest is only possible for a Dy-rich particle size below 3.5 μm, or 70% of the Dy-free grain size. Above this value, the desired microstructure is not possible which is why a part of the domain is hatched. Below this value, the size of the area of interest is growing and is shifted to smaller treatment times, pointing to the need for reduced diffusion durations. A qualitatively similar result is observed at an increased sintering temperature; only the thickness of the process windows is smaller because the diffusion kinetics are higher (Figure 6f).

### 3. Discussion

With the standard elaboration process implemented in this study, we manage to fabricate dense magnets with good magnetic properties. It is indeed commonly observed that using recycled materials in such a process can induce a decreased density<sup>[8,21,28]</sup> due to the incorporation of oxygen and carbon contaminated powders. This drawback is overcome here using only a

fraction of recycled powder and a specially designed RE-rich (33.5 wt%) virgin material SC alloy, in order to obtain a sufficient amount of liquid phase during the liquid-phase sintering stage. The remanence of our RE-rich alloys (in the 1.3 T range) is quite low compared to typical Nd–Fe–B values which can reach 1.49 T for N55 grade, but the use of RE-rich alloys, in turn, provides the possibility to increase the liquid phase fraction and thus decrease the sintering temperatures for a better control of the Dy diffusion. As expected, the coercivity of the produced magnets is enhanced with Dy addition, compared to the reference Dy-free magnet, up to 160 kA m<sup>-1</sup> wt%<sup>-1</sup> (Table 2). Similar performances can be obtained by a direct alloying of Dy in the alloy fabrication.<sup>[36]</sup> Moreover magnets produced by powder-blend methods having a core–shell microstructure exceed this value.<sup>[54,57]</sup> One reason for these relatively low magnetic performances could be the high level of impurities (C, O, and N) which are known to be detrimental to the magnetic properties.<sup>[21,72,73]</sup> No clear difference on the contamination levels was evidenced between the 5 and 3.5 μm batches. We are not in a position to propose an explanation for these *a priori* surprising results. For the same magnet fabrication process, the use of finer particles could have been expected to exacerbate reactivity issues due to an increased specific area. One point that should be noted in this respect is that these impurities were shown to come partly from the EoL magnets (Figure 1e). It should be accepted that top notch magnetic properties cannot be expected from a recycling process based on the use of EoL magnets. On a different line of thought, we saw also that decreasing the diffusion kinetics of Dy by decreasing the sintering temperature did not affect the coercivity gain per Dy unit mass, but systematically decreased the magnet SQ factor. This can tentatively be attributed to a more disperse grain size distribution as grain growth is limited at lower sintering temperatures.<sup>[74]</sup> Larger grains are generally less coercive and their magnetization reverses at lower fields than small grains.<sup>[75]</sup> They also impose higher volumetric reverse fields at their vicinities which can explain the SQ factor decrease. Another important element is that the annealing heat treatment was optimized for the main powder, which has a slightly different composition compared to recycled magnets (Table 3). It is possible that another annealing cycle would conduct to further increase the coercivity of the magnets.

Scanning electron microscope (SEM) microstructural characterization exhibited a quite homogeneous mixture despite an occasionally observed local agglomeration of recycled grains (Figure 2). We may then assume that this does not affect the magnetic properties of the elaborated magnets. At a grain scale however, microstructural analysis revealed that light core–shell effects could be distinguished on initial main powder grains, but they were also correlated to a clear anticore–shell effect (Figure 3). As these structures are known to be detrimental to coercivity development,<sup>[71]</sup> we may assume that they are also

**Table 3.** Compositions of starting materials. B, Al, Fe, Co, Cu, Ga, Pr, Nd, Dy analyzed by ICP [wt%], O, N, H and C, S by IGA [wt ppm].

Alloy	B	Al	Fe	Co	Cu	Ga	Pr	Nd	Dy	RE	O	N	H	C	S
SC	0.99	0.22	65	0.49	0.12	0.15	7.2	26.3	0.1	33.5	160 ± 30	13 ± 7	14 ± 6	180 ± 30	28 ± 2
M	1.1	0.53	67	0.51	0.09	0.05	6.8	22.2	4.5	33.5	3 900 ± 450	310 ± 30	30 ± 6	600 ± 70	20 ± 5

responsible for the low coercivity gains obtained. In order to understand how these microstructures appear, we need to consider the Dy transport mechanisms proposed in the literature (fusion/precipitation, CILFM, and diffusion). A clear effect due to the mixing ratio is a stability of the overall grain size and possibly a light decrease with decreasing EoL magnet powder size (Figure 2e). An explanation could be that more oxides present because of the use of recycled materials brings more pinning of the grain boundary motion, which slows down grain growth.<sup>[76]</sup> Judging from comparable powder blend methods where CILFM (or solution/precipitation) could account for the Dy shell formation, a significant grain growth correlated to Dy incorporation should be observed on final magnets.<sup>[54,59]</sup> The fact that this is not the case here might exclude these mechanisms on magnet scale. However, the presence of sharp interfaces on anticore-shell recycled grains suggests that a fusion/precipitation of Dy-poor shells<sup>[68]</sup> or CILFM is locally possible. In order to consider the global Dy transport, these observations encouraged us to

study what a dual liquid and solid diffusion can explain in the Dy transport with finite element simulations.

The quite simple diffusion model used, which considers only the solid and liquid diffusion existing coefficients, can describe some features of the observed microstructures. A first result is that the diffusion coefficients in the liquid are high enough to consider that the Dy concentration of the liquid phase is spatially uniform, so that the diffusion kinetics are governed by the solid-state diffusion. These simulations show that, if the grain size is similar for the two powders, it is possible to find either a homogeneous distribution or a core-shell + anticore-shell type structure (Figure 6c). This is far from the ideal shell which is nm thick and highly Dy-rich in the vicinity of grain boundaries, where reverse stray fields nucleate preferentially.<sup>[77]</sup> But starting from recycled powders, it is impossible with this method to control the initial microstructure of the grains as well as their Dy-concentration. In our case, our attempt to decrease the particle size of the recycled powders did not affect the coercivity gain per

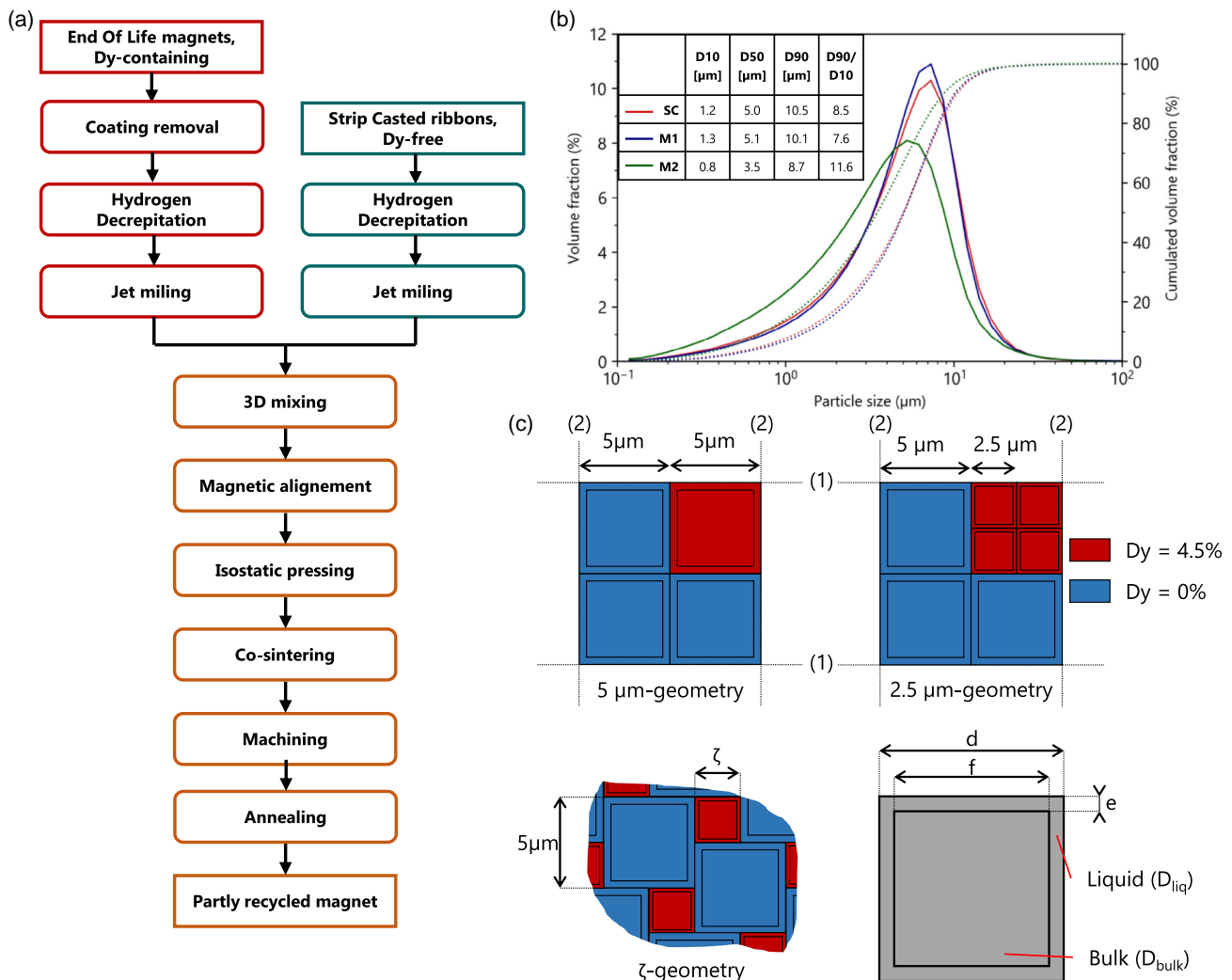


**Figure 7.** a) Experimental approach showing the manufacturing. b) Particle size distribution and cumulated volume fraction after jet-milling of SC alloy, and M alloy for two different D50 (5 and 3.5 μm). c) Schematic representation of the Dy-rich (red) and Dy-free (blue) grains in the initial state of the simulation with periodic boundary conditions. Each solid grain is cubic with  $d$  size and perfectly wetted by a liquid film of thickness  $e$ .

Dy unit mass (Table 2), but decreased the SQ factor especially for the 975 °C–6 h batches (Figure 1c,d). This can be attributed to a larger D90/D10 ratio (Figure 7b) which reached 11.6 compared to 7.6 for M1 batch. An explanation for this is that grain size of the M magnet was around 5 μm (see Section 5) which means that decreasing the grain size of the jet-milled particles is done by eroding Nd<sub>2</sub>Fe<sub>14</sub>B grains, which may result in a wider particle size distribution. But the only way to avoid the formation of this anticore–shells and thus limit the use of critical HRE should be, according to our model, to reduce the initial particle size of the recycled grains. The estimated particle size should be below 70% of the main powder particle size in order to get an homogeneous concentration in the initially Dy-rich grain and a clear core–shell structure in the main grains (Figure 6e). With an average particle size of 3.5 μm for the SC-M2 batch, it is, according to our model, impossible to explain the achievement of an ideal microstructure which is consistent with the observations on our samples (Figure 3).

The best magnetic properties were obtained with sintering at 1050 °C–4 h, which, according to our model, leads to a total homogenization of the Dy concentration. However, EDS concentrations (Figure 3f,g) suggests that Dy concentration is still heterogeneous. Our model can then not fully account for the obtained microstructures and several explanations can be proposed. A first obvious one is that diffusion coefficients values are not very accurate due to a lack of reliable experimental data. To illustrate this point of sensitivity to the input diffusivity data, we see from Figure 6c that a duration of only 1.0 h is necessary to reach total homogenization for a temperature of 1050 °C ( $D_{\text{bulk}} = 2.9 \times 10^{-16} \text{ m}^2 \text{ s}^{-1}$ ). For a temperature of 1000 °C, 3.1 h is required, corresponding to a time factor of 3 for a 67% relative difference in the solid diffusion coefficient. Of course, diffusion in itself exhibits an equivalence between several temperatures/durations which does not account for other microstructural aspects. For instance, a decreased diffusion temperature allows a wider range of durations explaining the formation of core–shells, but we demonstrated that it was also correlated to a decreased SQ due to a wider grain size distribution. In addition, initial conditions of the model exhibit quite abrupt concentration gap, and the hypothesis of total wetting of the grains might be unrealistic at the studied temperatures according to Straumal et al.<sup>[61]</sup> But this perfect wetting might as well locally not occur due of the presence of oxides at grain boundaries. During liquid phase sintering, a macroscopic transport could then occur, with rearrangement, dissolution-precipitation, and grain growth.<sup>[74]</sup> This should also affect Dy transport even though the formation of the shells is, in this process a local phenomenon. In this regard, full densification is complete only after a certain time and remaining porosities might be diffusion obstacles to Dy diffusion and imply an underestimation of the diffusion durations. The presence of oxides is known to decrease Dy diffusion kinetics<sup>[78]</sup> because it decreases the liquid phase fraction. But this liquid phase fraction did not affect the results of the simulation as it should have an impact at least on densification kinetics and hence on transport kinetics. We might also consider, as an outlook, that Dy diffusion into Nd<sub>2</sub>Fe<sub>14</sub>B phase is known to be anisotropic depending on crystallographic axis,<sup>[40,79,80]</sup> whereas the model here is completely isotropic. Last but not least is that we did not take into account local equilibrium at the liquid/solid

interface. Indeed, the concentration there is considered constant, but we should expect a partition coefficient between Nd and Dy between the liquid and the solid, as well as a saturation concentration of RE in the liquid as predicted in the Nd–Fe–B phase diagram.<sup>[81]</sup> These effects may also govern the transport kinetics. To verify this hypothesis, concentration profiles on the grain and estimations of the partition coefficients would possibly pave the way to a better understanding of Dy transport in such a process. Despite these numerous limitations, the main conclusion of the model will probably not change: significantly smaller Dy-rich particles compared to Dy-poor should be used to achieve an ideal microstructure.

## 4. Conclusion

In this study, a recycling process of HRE-rich EoL permanent magnets was implemented with the goal to use them as the only source of HRE, and to localize the HRE in the vicinity of grain boundaries of the φ-phase in a partly recycled sintered magnet. It was shown that full density magnets with satisfactory magnetic properties were obtained (example:  $B_r = 1.25 \pm 0.04 \text{ T}$  and  $H_{cJ} = 1625 \pm 30 \text{ kA m}^{-1}$ ). However, the coercivity gain per Dy unit mass up to  $160 \pm 30 \text{ kA m}^{-1} \text{ wt}\%^{-1}$  was seen to be quite low compared to methods allowing an efficient use of HRE. Apart from the potential effect of the observed increase amount of impurities in the sintered magnet, an explanation for this is that a significant amount of Dy remains stuck in the initial recycled particle and does not contribute to the coercivity improvement.

The observed formation of anticore–shells in recycled Dy-rich grains correlated to core–shells in initially Dy-free grains was qualitatively explained by a numerical diffusion model. This model showed that a reduction of the Dy-rich particles below 70% of the main powder particle can in some cases lead to an ideal configuration, where the majority of the Dy initially present in Dy-rich particles diffuses to form a core–shell on the initially Dy-free grains. However, the achievement of such an ideal microstructure may be difficult in practice because it would require the use of very small (say in the 1–2 μm range for a 5 μm main powder) with associated pollution and microstructural issues. This study emphasized that a model based on diffusive transport can qualitatively account for the observed microstructure, compared to other known mechanisms for shell formation (melting/precipitation and CILFM).

However, on a quantitative basis, the model does not fit correctly our experimental results. This could be due *inter alia* to the use of inadequate diffusivity data, as the literature on the topic is unfortunately scarce. In this context, a first obvious perspective of the present work would be to set up an experimental program aiming at the determination of the solid diffusion coefficients and their temperature dependence. Regarding the numerical model, another perspective would be to take into account other physical phenomena occurring during liquid phase sintering. And from an experimental standpoint, despite the aforementioned issues, an interesting perspective would be to fabricate magnets with Dy-rich grains in the μm range out of recycled materials.

## 5. Experimental Section

**Starting Materials:** Strip cast Dy-free alloy (SC) and a 30 kg batch of Dy-rich EV engine sintered magnets (M) were used for this study ( $B_r = 1.22 \pm 0.04$  T,  $H_{cJ} > 1800$  kA m<sup>-1</sup>). The phosphorous-based coating of the EoL magnet was mechanically removed. Their compositions are given in Table 3. The B, Al, Fe, Co, Cu, Ga, Pr, Nd, and Dy contents were measured by the inductively coupled plasma (ICP) optical emission spectroscopy (725 AGILENT), with an expected uncertainty of  $\pm 5\%$  in relative terms. As for O, N, H and C, S their contents were measured by instrumental gas analyzer (IGA) technique (HORIBA EMGA and EMIA IGA), the error bars reported in Table 3 representing the statistical dispersion on a set of three experiments. The EoL magnets M have a grain size of  $4.0 \pm 0.3$  and  $5.7 \pm 1.3$   $\mu\text{m}$  measured by linear intercept method along and perpendicular to  $c$ -axis, respectively.

**Magnets Manufacturing:** Batches of 3 kg of SC ribbons and EoL magnets were separately hydrogen decrepitated at 50 °C and 2 bar of high-purity hydrogen that yielded coarse powders with particle sizes in the 100  $\mu\text{m}$ –1 mm range. After complete hydrogen absorption, partial hydrogen desorption steps were applied at 250 and 550 °C under primary vacuum during 60 and 90 min, respectively. The coarse powders were separately jet-milled under nitrogen gas, and the targeted particle size was controlled by an in-line Malvern laser diffraction granulometer. Three batches were prepared: SC (D50 = 5  $\mu\text{m}$ ) for the strip cast alloy, M1 (D50 = 5  $\mu\text{m}$ ), and M2 (D50 = 3.5  $\mu\text{m}$ ) for the recycled magnets. Blending of jet-milled powders (SC-M1 and SC-M2) was implemented with a Turbula T10B 3D mixer (35 rpm, 1 h) with recycled powder mass ratios ranging from 0 to 50 wt%. Reference magnets, made only with SC powder, as well as magnets consisting partially of recycled materials were fabricated using the standard powder metallurgy route. Anisotropy was obtained by aligning the jet-milled powder in magnetic field with magnetic pulse cycles reaching 6 T. Green compacts were obtained by cold isostatic pressing under 150 MPa. Subsequently, the complete degassing of hydrogen was performed at 750 °C during 2 h, followed by a 2.5 °C min<sup>-1</sup> ramp to reach the sintering plateau, ranging from 975 to 1050 °C for durations of 4–6 h in a secondary vacuum furnace. After quenching, machining enabled to obtain cylinders of 7 mm height and 10 mm diameter. A postsintering annealing treatment at 800–850 °C and 520 °C with 2 h dwell time, previously optimized for the reference Dy-free magnets, enabled the coercivity enhancement. The experimental magnet manufacturing process is summarized on Figure 7a. Particle size distributions after jet-milling of SC, M1, and M2 batches are given in Figure 7b.

**Characterizations:** Apparent density of the obtained magnets was measured using Archimedes method. As for the starting magnets, O, N, H and C, S contents were measured by IGA. The demagnetizing curves of the sintered magnets were measured using a closed-loop B-H tracer (Laboratorio Elettrofisico LEP/200-4S). SQ factor was defined as  $H_k/H_{cJ}$  with  $H_{cJ}$  the magnet's coercivity and  $H_k$  the reverse external applied field necessary to reach 90% of the remanence. Microstructural analysis was performed with high-resolution Zeiss Merlin Gemini-2 SEM in secondary electrons and BSE modes on resin embedded polished surfaces. The microscope was equipped with two EDS detectors (Bruker QUANTAX—XFlash6). Semiquantitative spectra, elemental profiles, and maps were acquired at 10 kV with a 10 mm working distance, and the data were analyzed with Esprit 2.3 software. Elemental maps were presented with a smoothing factor of 3 of this software to enhance visibility. Grain sizes were determined by surface analysis considering each grain as a sphere with the same section (200–300 grains were counted for each sample). The mean diameter of the grain sections was then multiplied by 1.571 to estimate the spatial diameter of the corresponding tetradehedron using the ASTM E112 “Standard Test Methods for Determining Average Grain Size” norm.<sup>[82]</sup>

**Simulations:** Finite element diffusion simulations solving Fick's second law (1) were performed on COMSOL Multiphysics 6.0 with diluted elements physics. Transport was modeled with a homogeneous isotropic diffusion coefficient  $D_{\text{bulk}}$  for the bulk solid and  $D_{\text{liq}}$  for the liquid. These diffusion coefficients were calculated for each temperature with an Arrhenius law (2) using existing data for the bulk diffusion<sup>[83,84]</sup>

( $Q = 315$  kJ mol<sup>-1</sup>,  $D_0 = 8.10^{-4}$  m<sup>2</sup> s<sup>-1</sup>). Similarly, liquid diffusion coefficient was estimated from the data of liquid diffusion of Dy in a Dy-free magnet<sup>[38]</sup> ( $D = 8.45 \times 10^{-11}$  m<sup>2</sup> s<sup>-1</sup>). In the absence of specific literature data, the activation energy of the solid was also used for the liquid.<sup>[83]</sup>

The transport equations were solved in 2D on various square lattice pavements (Figure 7c). For an initially solid square of size  $d$ , the liquid phase fraction  $f(T)$  was calculated for each temperature using existing thermodynamic assessment of the Nd–Fe–B phase diagram<sup>[81]</sup> with Nd = 33.5 wt%. The amount of remaining solid phase was assumed to be a square of size  $f$  given from Equation (3) as if it was a scaled section of a 3D grain network. Finally, the thickness of the liquid film surrounding the grains was given as  $2e = d - f$ . In order to evaluate the relative influence of Dy diffusion lengths and the pattern size, two geometries with the same amount of Dy diffusing were tested in this study: a 5  $\mu\text{m}$  geometry with 1 Dy-rich 5  $\mu\text{m}$  grain (4.5 wt%) for 3 Dy-free 5  $\mu\text{m}$  grains, and a 2.5  $\mu\text{m}$  geometry with 4 Dy-rich 2.5  $\mu\text{m}$  grains for 3 Dy-free 5  $\mu\text{m}$  grains. Though apparently very similar these geometries differ by the existence of a denser network of liquid pathways for Dy transport in the 2.5  $\mu\text{m}$  geometry. To quantify the influence of the Dy-rich particle size on the evolution of the Dy concentration, other geometries allowing various Dy-rich particle sizes ( $\zeta$  geometry) were tested. At the initial state, each grain was considered as perfectly wetted by the liquid and in perfect contact with the other grains. The initial state and the geometries are summarized in Figure 7c. Periodic boundary conditions were used along the (1), (2) axes. These simulations can be run on a standard laptop.

$$\frac{\partial c}{\partial t} = D \cdot \Delta c \quad (1)$$

$$D(T) = D_0 e^{-\frac{Q}{RT}} \quad (2)$$

$$f = d \sqrt[3]{1 - f(T)} \quad (3)$$

## Supporting Information

Supporting Information is available from the Wiley Online Library or from the author.

## Acknowledgements

This work was partly funded by Orano group and Bpifrance within the MAGNOLIA project. We thankfully acknowledge the contribution of Hugo Daydé for the production of experimental results.

## Conflict of Interest

The authors declare no conflict of interest.

## Data Availability Statement

The data that support the findings of this study are available from the corresponding author upon reasonable request.

## Keywords

core–shells, grain boundary diffusion, Multi Main Phase, Nd–Fe–B magnets, rare earths, recycling, resource criticality

Received: February 16, 2024  
Published online: March 21, 2024



- [1] M. Sagawa, S. Fujimura, N. Togawa, H. Yamamoto, Y. Matsuura, *J. Appl. Phys.* **1984**, 55, 2083.
- [2] J. J. Croat, J. F. Herbst, R. W. Lee, F. E. Pinkerton, *J. Appl. Phys.* **1984**, 55, 2078.
- [3] O. Gutfleisch, M. A. Willard, E. Brück, C. H. Chen, S. G. Sankar, J. P. Liu, *Adv. Mater.* **2011**, 23, 821.
- [4] R. Gauß, C. Burkhardt, F. Carencotte, M. Gasparon, O. Gutfleisch, I. Higgins, M. Karajić, A. Klosek, M. Mäkinen, B. Schäfer, R. Schindler, B. Veluri, *Rare Earth Magnets and Motors: A European Call for Action* **2021**, [https://eit.europa.eu/sites/default/files/2021\\_09-24\\_ree\\_cluster\\_report2.pdf](https://eit.europa.eu/sites/default/files/2021_09-24_ree_cluster_report2.pdf).
- [5] S. Constantinides, *Arnold Magnetic Technologies, Techniqal Review*, Vol. 150903a, **2015**, <https://www.arnoldmagnetics.com/wp-content/uploads/2017/10/Important-Role-of-Dysprosium-in-Modern-Permanent-Magnets-150906.pdf>.
- [6] Y. Yang, A. Walton, R. Sheridan, K. Güth, R. Gauß, O. Gutfleisch, M. Buchert, B.-M. Steenari, T. Van Gerven, P. T. Jones, K. Binnemans, *J. Sustainable Metall.* **2017**, 3, 122.
- [7] S. Rivoirard, J. G. Noudem, P. De Rango, D. Fruchart, S. Liesert, J. L. Soubeyrou, in *Proc. of the 16th int. Workshop on Rare-Earth Magnets and Their Applications*, Sendai Japan **2000**, p. 347.
- [8] M. Zakotnik, E. Devlin, I. R. Harris, A. J. Williams, in *Proc. 19th Int. Workshop on Rare Earth Permanent Magnets & Their Applications*, Grenoble France, Vol. 1, **2004**, p. 267.
- [9] B. Michalski, M. Szymanski, K. Gola, J. Zygmuntowicz, M. Leonowicz, *J. Magn. Magn. Mater.* **2022**, 548, 168979.
- [10] M. Kimiabeigi, R. S. Sheridan, J. D. Widmer, A. Walton, M. Farr, B. Scholes, I. R. Harris, *IEEE Trans. Ind. Electron.* **2018**, 65, 3795.
- [11] A. Lixandru, I. Poenaru, K. Güth, R. Gauß, O. Gutfleisch, *J. Alloys Compd.* **2017**, 724, 51.
- [12] X. Li, M. Yue, M. Zakotnik, W. Liu, D. Zhang, T. Zuo, *J. Rare Earths* **2015**, 33, 736.
- [13] C. Li, M. Yue, W. Liu, T. Zuo, X. Yi, J. Chen, Z. Zhou, Y. Wu, *J. Mater. Cycles Waste Manage.* **2015**, 17, 547.
- [14] A. Walton, H. Yi, N. A. Rowson, J. D. Speight, V. S. J. Mann, R. S. Sheridan, A. Bradshaw, I. R. Harris, A. J. Williams, *J. Cleaner Prod.* **2015**, 104, 236.
- [15] R. S. Sheridan, A. J. Williams, I. R. Harris, A. Walton, *J. Magn. Magn. Mater.* **2014**, 350, 114.
- [16] O. Gutfleisch, K. Güth, T. G. Woodcock, L. Schultz, *Adv. Energy Mater.* **2013**, 3, 151.
- [17] R. S. Sheridan, R. Sillitoe, M. Zakotnik, I. R. Harris, A. J. Williams, *J. Magn. Magn. Mater.* **2012**, 324, 63.
- [18] J. J. Luo, P. de Rango, D. Fruchart, J. N. Mei, L. Zhou, *J. Alloys Compd.* **2011**, 509, 4252.
- [19] M. Zakotnik, I. R. Harris, A. J. Williams, *J. Alloys Compd.* **2008**, 450, 525.
- [20] T. Kawasaki, M. Itoh, K. Machida, *Mater. Trans.* **2003**, 44, 1682.
- [21] M. Schönfeldt, U. Rohrmann, P. Schreyer, M. Hasan, K. Opelt, J. Gassmann, A. Weidenkaff, O. Gutfleisch, *J. Alloys Compd.* **2023**, 939, 168709.
- [22] P. A. Prokofev, N. B. Kolchugina, K. Skotnicova, G. S. Burkhanov, M. Kursa, M. V. Zheleznyi, N. A. Dormidontov, T. Cegan, A. S. Bakulina, Y. S. Koshkidko, B. Smetana, *Materials* **2020**, 13, 3049.
- [23] H. Sepehri-Amin, T. Ohkubo, M. Zakotnik, D. Prosperi, P. Afunoy, C. O. Tudor, K. Hono, *J. Alloys Compd.* **2017**, 694, 175.
- [24] W. Ji, W. Liu, M. Yue, D. Zhang, J. Zhang, *Phys. B: Condens. Matter* **2015**, 476, 147.
- [25] M. Zakotnik, C. O. Tudor, *Waste Manage.* **2015**, 44, 48.
- [26] W. Liu, C. Li, M. Zakotnik, M. Yue, D. Zhang, X. Huang, *J. Rare Earths* **2015**, 33, 846.
- [27] C. Li, W. Q. Liu, M. Yue, Y. Q. Liu, D. T. Zhang, T. Y. Zuo, *IEEE Trans. Magn.* **2014**, 50, 12.
- [28] M. Zakotnik, I. R. Harris, A. J. Williams, *J. Alloys Compd.* **2009**, 469, 314.
- [29] O. Diehl, M. Schönfeldt, E. Brouwer, A. Dirks, K. Rachut, J. Gassmann, K. Güth, A. Buckow, R. Gauß, R. Stauber, O. Gutfleisch, *J. Sustainable Metall.* **2018**, 4, 163.
- [30] X. T. Li, M. Yue, W. Q. Liu, X. L. Li, X. F. Yi, X. L. Huang, D. T. Zhang, J. W. Chen, *J. Alloys Compd.* **2015**, 649, 656.
- [31] H. Sepehri-Amin, S. Hirose, K. Hono, *Handbook of Magnetic Materials*, Vol. 27, Elsevier **2018**, pp. 269–372, <https://doi.org/10.1016/bs.hmm.2018.08.003>.
- [32] K. Hono, H. Sepehri-Amin, *Scr. Mater.* **2012**, 67, 530.
- [33] M. Lv, T. Kong, W. Zhang, M. Zhu, H. Jin, W. Li, Y. Li, *J. Magn. Magn. Mater.* **2021**, 517, 167278.
- [34] T. Helbig, K. Loewe, S. Sawatzki, M. Yi, B.-X. Xu, O. Gutfleisch, *Acta Mater.* **2017**, 127, 498.
- [35] Z. Wang, T. T. Sasaki, Y. Une, T. Ohkubo, K. Hono, *Acta Mater.* **2023**, 248, 118774.
- [36] Z. Wang, Y. Li, H. Wu, M. Ji, H. Zhang, W. Liu, M. Yue, *J. Alloys Compd.* **2023**, 943, 169174.
- [37] T.-H. Kim, T. T. Sasaki, T. Ohkubo, Y. Takada, A. Kato, Y. Kaneko, K. Hono, *Acta Mater.* **2019**, 172, 139.
- [38] K. Loewe, D. Benke, C. Kübel, T. Lienig, K. P. Skokov, O. Gutfleisch, *Acta Mater.* **2017**, 124, 421.
- [39] H. Sepehri-Amin, T. Ohkubo, K. Hono, *Acta Mater.* **2013**, 61, 1982.
- [40] T.-H. Kim, S.-R. Lee, S. J. Yun, S. H. Lim, H.-J. Kim, M.-W. Lee, T.-S. Jang, *Acta Mater.* **2016**, 112, 59.
- [41] L. Zhao, J. He, W. Li, X. Liu, J. Zhang, L. Wen, Z. Zhang, J. Hu, J. Zhang, X. Liao, K. Xu, W. Fan, W. Song, H. Yu, X. Zhong, Z. Liu, X. Zhang, *Adv. Funct. Mater.* **2022**, 32, 2109529.
- [42] Z. Wang, M. Yue, W. Liu, Y. Li, H. Wu, Y. Liu, S. Zha, X. Yi, D. Zhang, Q. Lu, H. Zhang, *Scr. Mater.* **2022**, 217, 114789.
- [43] R. S. Mottram, A. Kianvash, I. R. Harris, *J. Alloys Compd.* **1999**, 283, 282.
- [44] A. Kianvash, R. S. Mottram, I. R. Harris, *J. Alloys Compd.* **1999**, 287, 206.
- [45] G. Yan, P. J. McGuinness, J. P. G. Farr, I. R. Harris, *J. Alloys Compd.* **2010**, 491, L20.
- [46] T.-H. Kim, S.-R. Lee, H.-J. Kim, M.-W. Lee, T.-S. Jang, *Acta Mater.* **2015**, 93, 95.
- [47] P. Liu, T. Ma, X. Wang, Y. Zhang, M. Yan, *J. Alloys Compd.* **2015**, 628, 282.
- [48] A. M. Gabay, M. Marinescu, W. F. Li, J. F. Liu, G. C. Hadjipanayis, *J. Appl. Phys.* **2011**, 109, 083916.
- [49] K. Skotnicova, G. S. Burkhanov, N. B. Kolchugina, M. Kursa, T. Cegan, A. A. Lukin, O. Zivotsky, P. A. Prokofev, J. Jurica, Y. Li, *J. Magn. Magn. Mater.* **2020**, 498, 166220.
- [50] K. Skotnicova, P. A. Prokofev, N. B. Kolchugina, G. S. Burkhanov, A. A. Lukin, Y. S. Koshkid'ko, T. Cegan, H. Drulis, T. Romanova, N. A. Dormidontov, *Materials* **2019**, 12, 4235.
- [51] Z. Li, Z. Zhang, Y. Fu, C. Wang, L. Wei, S. Bai, *J. Alloys Compd.* **2022**, 926, 166944.
- [52] Y. Qin, W. Liu, Z. Li, H. Chen, H. Wu, Z. Guo, T. Yang, Y. Li, M. Yue, *Intermetallics* **2022**, 149, 107679.
- [53] P. Zhang, W. Sun, J. Wang, B. Li, W. Xia, H. Liu, Y. Wang, Y. Cao, G. Xu, Y. Wu, *J. Supercond. Novel Magn.* **2022**, 35, 491.
- [54] K. Opelt, T. Ahmad, O. Diehl, M. Schönfeldt, E. Brouwer, I. Vogel, J. D. Rossa, J. Gassmann, S. Ener, O. Gutfleisch, *Adv. Eng. Mater.* **2021**, 23, 2100459.
- [55] X. Liu, M. Pan, P. Zhang, T. Ma, L. Zhao, L. Li, *J. Rare Earths* **2021**, 39, 558.
- [56] T. Zhou, P. Qu, W. Pan, R. Li, M. Li, S. Ur Rehman, Z. Zhong, G. Xie, *J. Alloys Compd.* **2021**, 856, 158191.

- [57] L. Yuping, W. Mengling, L. Jiayu, *J. Mater. Sci.: Mater. Electron.* **2020**, 31, 7211.
- [58] Z. Zhang, H. Chen, J. Jin, B. Lim, X. Liu, W. Li, M. Yan, S. P. Ringer, *Acta Mater.* **2023**, 261, 119344.
- [59] D. Liu, J. Xiong, L. Wang, X. Zheng, F. Peng, X. Ming, T. Zhao, F. Hu, J. Sun, B. Shen, J. Shen, *Acta Mater.* **2023**, 246, 118710.
- [60] R. Gauß, O. Diehl, E. Brouwer, A. Buckow, N. Groth, K. Güth, M. Schönfeldt, K. Rachut, A. Dirks, J. Gassmann, R. Hord, R. Stauber, O. Gutfleisch, in *24th Int. Workshop on Rare-Earth and Future Permanent Magnets and Their Applications*, Darmstadt, Deutschland **2016**, pp. O14–1630.
- [61] B. B. Straumal, Yu. O. Kucheev, I. L. Yatskovskaya, I. V. Mogilnikova, G. Schütz, A. N. Nekrasov, B. Baretzky, *J. Mater. Sci.* **2012**, 47, 8352.
- [62] H. Nakamura, K. Hirota, M. Shimao, T. Minowa, M. Honshima, *IEEE Trans. Magn.* **2005**, 41, 3844.
- [63] W. Song, J. He, H. Pan, Z. Yu, J. Cao, W. Fan, H. Yu, Z. Liu, *Mater. Lett.* **2022**, 328, 133207.
- [64] B. Wu, X. Ding, Q. Zhang, L. Yang, B. Zheng, F. Hu, Z. Song, *Scr. Mater.* **2018**, 148, 29.
- [65] H. Zeng, Z. Liu, W. Li, J. Zhang, L. Zhao, X. Zhong, H. Yu, B. Guo, *J. Magn. Magn. Mater.* **2019**, 471, 97.
- [66] K. Löewe, C. Brombacher, M. Katter, O. Gutfleisch, *Acta Mater.* **2015**, 83, 248.
- [67] J. Fliegans, C. Rado, R. Soulas, L. Guetaz, O. Tsononi, N. M. Dempsey, G. Delette, *J. Magn. Magn. Mater.* **2021**, 520, 167280.
- [68] U. M. R. Seelam, T. Ohkubo, T. Abe, S. Hirosawa, K. Hono, *J. Alloys Compd.* **2014**, 617, 884.
- [69] T.-H. Kim, T. T. Sasaki, T. Koyama, Y. Fujikawa, M. Miwa, Y. Enokido, T. Ohkubo, K. Hono, *Scr. Mater.* **2020**, 178, 433.
- [70] N. Oono, M. Sagawa, R. Kasada, H. Matsui, A. Kimura, *J. Magn. Magn. Mater.* **2011**, 323, 297.
- [71] X. Liu, J. He, B. Yuan, Z. Liu, *Appl. Phys. A* **2023**, 129, 619.
- [72] T. T. Sasaki, T. Ohkubo, Y. Une, H. Kubo, M. Sagawa, K. Hono, *Acta Mater.* **2015**, 84, 506.
- [73] T. Crozier-Bioud, V. Momeni, J. Gonzalez-Gutierrez, C. Kukla, S. Luca, S. Rolere, *Mater. Today Phys.* **2023**, 34, 101082.
- [74] R. M. German, P. Suri, S. J. Park, *J. Mater. Sci.* **2009**, 44, 1.
- [75] R. Ramesh, K. Srikrishna, *J. Appl. Phys.* **1988**, 64, 6406.
- [76] S. Namkung, D. H. Kim, T. S. Jang, *Rev. Adv. Mater. Sci.* **2011**, 28, 185.
- [77] T. Oikawa, H. Yokota, T. Ohkubo, K. Hono, *AIP Adv.* **2016**, 6, 056006.
- [78] K.-H. Bae, S.-R. Lee, H.-J. Kim, M.-W. Lee, T.-S. Jang, *J. Appl. Phys.* **2015**, 118, 203902.
- [79] E. Niu, Z.-A. Chen, X.-Z. Ye, W. Zhu, G.-A. Chen, Y.-G. Zhao, J. Zhang, X.-L. Rao, B.-P. Hu, Z.-X. Wang, *Appl. Phys. Lett.* **2014**, 104, 262405.
- [80] W. Li, Q. Zhou, L. Z. Zhao, Q. X. Wang, X. C. Zhong, Z. W. Liu, *J. Magn. Magn. Mater.* **2018**, 451, 704.
- [81] B. Halleman, P. Wollants, J. R. Roos, *J. Phase Equilib.* **1995**, 16, 137.
- [82] E04 Committee, *US Dpt of Defense, ASTM E112-13 International*, 10.1520/E0112-13R21 **2021**.
- [83] M. F. De Campos, *Mater. Sci. Forum* **2012**, 727–728, 163.
- [84] B. A. Cook, J. L. Harringa, F. C. Laabs, K. W. Dennis, A. M. Russell, R. W. McCallum, *J. Magn. Magn. Mater.* **2001**, 233, 136.